ADVANCED MATERIALS FOR ENERGY & APPLICATIONS

Photocatalytic dye degradation and antibacterial activities of CeO$_2$/g-C$_3$N$_4$ nanomaterials for environmental applications

Sachin Shoran[1] · Sudesh Chaudhary[1] · Anshu Sharma[2]

Abstract

The uncontrolled dumping of synthetic dyes into water sources has posed severe hazards to the ecosystem. For decades, several materials with low cost and high efficiency have been investigated for dye degradation. Photocatalytic degradation is regarded as a successful strategy since it utilizes sunlight to transform harmful pollutants into nontoxic compounds without using oxidative agents. The photocatalytic potentials of CeO$_2$/g-C$_3$N$_4$ (CG) were investigated in this work using a simplistic ultrasonication process. Here, the amount of CeO$_2$ was fixed, and g-C$_3$N$_4$ was varied in the ratio (1:x, where x = 1, 2, and 3) and abbreviated as CG1, CG2, and CG3. Characterization techniques such as Fourier transforms-infrared spectroscopy, thermal gravimetric analysis (TGA), powdered X-ray diffraction, ultraviolet–visible spectroscopy, etc. were used to characterize structural analysis, optical properties, particle size, and chemical bonds of the prepared nanocomposites. The photocatalytic results showed that CG2 effectively degraded rose bengal (RB) and crystal violet (CV) dyes when exposed to visible light irradiation as compared to pure GCN and CeO$_2$. The antibacterial activity analysis further supported the potential application of prepared photocatalyst as a disinfectant agent against both gram-positive (*Staphylococcus aureus* and *Bacillus cereus*) and gram-negative (*Salmonella abony* and *Escherichia coli*) pathogenic strains of bacteria.

Keywords Photocatalyst · CeO$_2$/g-C$_3$N$_4$ · Rose bengal · Crystal violet · Dye degradation

Introduction

In the current global scenario, environmental pollution is a worldwide issue that is inextricably linked to rapid industrialization, raising concerns on how to further solve the energy dilemma in various modes and capacities. To enhance the application of solar energy, photocatalysis has become a versatile and promising benchmark in research and effective industrial management. The concerned photocatalyst should be activated and regulated to incur minimal economic and environmental costs while proving a potent solution for metallic or toxic elements causing secondary pollution. On the basis of recent trends, photocatalysis has become widely accepted as a green technology to treat polluted water. It is also noticed that the advancement of photocatalytic activity was hampered by the lack of highly efficient photocatalysts and classic reactors. The stable and consistent metal oxide photocatalyst "TiO$_2$" typically has negligible visible light absorption due to its colossal bandgap (Dette et al. 2014), which may not fulfill the demands for the accurate objective to be achieved. To find a solution to the issue, many other approaches have been tried, such as decreasing the particle size (Retamoso et al. 2019), loading it with nonmetal (Mittal et al. 2019), and mixing TiO$_2$ with another semiconductor (Pawar et al. 2018). Consequently, the development of a photocatalyst that is effective under visible light is still desirable on the note of making use of solar energy.

As a photocatalyst, the graphitic carbon nitride (GCN) material has been developed for photocatalytic applications. It is an organic polymeric semiconductor material made up of carbon, nitrogen, and a minimal amount of

✉ Anshu Sharma
anshushsharda@gmail.com

Sudesh Chaudhary
sudesh.energy@dcrustm.org

[1] Center of Excellence for Energy and Environmental Studies, Deenbandhu Chhotu Ram University of Science and Technology, Murthal 131039, Haryana, India

[2] Department of Physics, School of Engineering and Technology, Central University of Haryana, Mahendergarh 123031, Haryana, India

hydrogen content (Ong et al. 2016). Additionally, the availability of the larger surface area of this GCN material is due to its 2D orientation with interlocking planes, which is quite similar to the graphite structure. The above compound is also undermined by its remarkable rate of reintegration of electron–hole pairs, photogenerated, leading to its tendency to create heterojunctions. It is found that in comparison to conventional catalysts, GCN has many benefits, including the non-exhibition of high thermal and chemical stability (Yuan et al. 2015), featuring an electronic structure that can be altered accordingly with being both plentiful and affordable. Many researchers are focusing on the graphitic carbon nitride's visible light response and superior thermal stability due to the fact that it demonstrates significant benefits in photocatalytic water splitting (Sharma et al. 2022), photodegradation of hazardous toxic compounds (Rattan Paul and Nehra 2021a), electrochemical sensing (Zou et al. 2018), and biomedical imaging; moreover, it has emerged amongst the most potentially beneficial photocatalysts. Apart from this, GCN also has some inevitable constraints, such as low quantum efficiency, a lesser specific surface area (Wu et al. 2014), an inability to absorb over 460 nm, lower active sites, etc., all of which contribute to the low photocatalytic activity. To these drawbacks, there have been many different approaches taken to refine the photocatalytic activity of graphitic carbon nitride when it is exposed to visible light. Some of these approaches include chemical doping with elements that are not native to the material (Paul et al. 2019), the prepping of novel nanostructures, the creation of a heterojunction composite with some other semiconductor, and so on.

It is found that CeO_2 is a potent photocatalyst, which absorbs light near the ultraviolet region and marginally in the visible region with a band gap ($Eg = 2.69$ eV). On considering the inherent properties of Ce, which are due to its rare availability along with its substantially stable oxide configurations, CeO_2, possesses highly decent oxidation reductive characteristics that make it suitable for a wide array of uses. As a result of the ability of Ce to coexist in two distinct oxidation states ($+ 3$ and $+ 4$) and its ease of switching between those states, it has become an extremely appealing candidate for the creation of oxygen vacancies. These vacancies make it possible to enhance surface properties (Khobragade et al. 2021), which can have a potential impact, particularly in catalysis, photocatalytic dye degradations (Channei et al. 2014) and hydrogen evolution (Song et al. 2021). When CeO_2 in synthetic structures can be regulated and produced effectively, it is likely that the composite materials could have some thrilling performances. Moreover, if CeO_2/GCN composites were designed for improvements to existing, it was upbeat that CeO_2/GCN composites could be a highly useful derivative.

To date, some research has been documented on CeO_2/GCN materials synthesized through different methods, such as template-assisted synthesis (Li et al. 2016), ultrasonic deposition (Saravanakumar et al. 2017), mixing-calcination route (Huang et al. 2013; Tan et al. 2015). Table 1 shows the comparison of previously reported work on CeO_2/GCN. However, to our knowledge, research on the effect of doping on the degradation of rose bengal and crystal violet dyes is limited for GCN-based composites. In this study, we developed a facile hydrothermal route of synthesizing GCN and CeO_2 using precursors like urea and cerrous nitrate hexahydrate, respectively, and then ultrasonically combined them in a fixed ratio. The physicochemical and electrochemical properties of the nanocomposites were studied using a variety of instrumental procedures. Experiments using photocatalysis have also been carried out with the goal of degrading organic dyes and analyzing antibacterial behavior against gram-positive bacteria (*Staphylococcus aureus* and *Bacillus cereus*) and gram-negative bacteria (*Salmonella abony* and *Escherichia coli*).

Table 1 Comparison of CeO2/g-C3N4 synthesis with previously reported works

Precursors		Method	Dyes degraded	Reference
CeO$_2$	g-C$_3$N$_4$			
Ceric ammonium nitrate	Dicyandiamide	Simple mixing-calcination	Methylene blue 4-chlorophenol	(Huang et al. 2013)
Cerium sulfate	Melamine	Ball milling	Methyl blue and rhodamine-B	(Subashini et al. 2021)
Cerium (III) chloride	Melamine	In situ	Diuron (herbicide)	(Kesarla et al. 2019)
CeO$_2$ powder	g-C$_3$N$_4$ powder	Mixing-calcination method	Ammonium perchlorate	(Tan et al. 2015)
Cerrous nitrate hexahydrate	Urea	Hydrothermal	Rose bengal Crystal violet	This work

Experimental details

Materials

Each initial reagent of an analytical grade purity was managed to obtain from SRL company sources and utilized without undergoing any additional purification; also, throughout the experiment distilled water was utilized.

Synthesis of GCN

The hydrothermal synthesis of bulk GCN was accomplished by using urea as a major contributor. In the synthesis process, 10 g of urea was placed in a ceramic crucible, thereby placed in a furnace at 550 °C for 3 h with a ramp rate of 5 °C/min. Finally, the obtained powder was dried and ground using a mortar.

Synthesis of CeO₂ nanoparticles

To synthesize CeO_2, firstly, in 19 mL of H_2O, 12.60 g of $Ce(NO_3)_3.6H_2O$ was added, and the mixture was stirred magnetically for almost 30 min, followed by ultrasonication for another 30 min. Injection of 0.5 mL of ammonium hydroxide (concentration = 50% *v/v*) was done to make the solution alkaline. Then, in an autoclave (50 mL), the mixture was sealed and kept in an oven for heating at 160 °C for exactly 12 h. Furthermore, the centrifugation of the product obtained was done along with its washing using ethanol and distilled water. Lastly, the product was placed in a hot air oven at 80 °C temperature for 6 h, followed by its heating in a muffle at 550 °C at a ramp rate of 5 °C for 3 h. Finally, grinded using a mortar-pestle to obtain even smaller particles.

Synthesis of CeO₂/GCN composites

Three distinct ratios of GCN and CeO_2 nanoparticles were collected, where CeO_2 was kept constant and GCN was altered in the ratio of 1:*x*, where *x* = 1, 2, and 3, respectively, and each mixture was ground in a pestle, followed by 30 min of ultrasonication, and dried for 8 h in a hot air oven at 60 °C. Finally, heating it in the furnace at a temperature of 550 °C for 3 h at a constant rate of 5 °C/min. resulted in the formation of desired CeO_2/ GCN composites, which are abbreviated as CG1, CG2, and CG3. Figure 1 shows the synthesis route of prepared nanocomposites.

Characterizations

The CeO_2/GCN nanocomposites in their crystallized phases were studied by XRD (X-ray diffraction) using a Bruker D8 diffractometer using Cu Kα radiation ($\lambda = 1.5418$ A) in the range of $2\theta = 20–80°$. Perkin Elmer spectrometer was used to record the FTIR (Fourier Transform infrared spectra) of the samples at the range 500–4000 cm⁻¹. A UV–Vis spectrophotometer (Shimadzu UV-2600 I) ranging between 400 and 800 nm was used to calculate ultraviolet–visible (UV–vis) diffuse reflection spectra in the laboratory setting. For structural and morphological analysis of the acquired samples, TEM (transmission electron microscopy) using Talos F200X and scanning electron microscopy (JSM 7900-F) were done. PerkinElmer 4000 was used for thermogravimetric studies. The heating range for TGA is from room temperature to 800 °C at a heating rate of 10 °C/min in the N_2 atmosphere. X-ray photoemission spectroscopy (XPS) spectra were measured on PerkinElmer LAMBDA 750 model with a monochromatic Mg Kα source to explore the elements on the surface. Photoluminescence spectra were measured on LS 55 (PerkinElmer). Electrochemical impedance spectroscopy (EIS) and cyclic voltammetry (CV) tests were done on Autolab PGSTAT204 Potentiostat.

The photocatalytic activity

The degradation of CV and RB dye in aqueous solutions in the photocatalytic reactor was used to evaluate the photoactivity of materials. The photocatalytic reactor was connected with two 200 W xenon lamps on the two opposing side walls to emulate solar irradiation. In a 250 mL conical flask container, 10 ppm of the dye solution and 0.01 g of the photocatalyst were used to conduct each experiment. To establish equilibrium, stirring of the solution was done for the next 30 min in the dark. After extracting 2 mL of the suspension, it was centrifuged quickly to separate out the photocatalyst. A UV–vis spectrophotometer (Shimadzu UV-2600 I) measured the visible spectrum absorption spectra of the drawn-out samples from 450 to 800 nm. Dye degradation was assessed by measuring the shift in main absorption peak intensity. Equation (1) used to compute the photocatalytic degradation efficiency is

$$E = \left(1 - C/C_0\right) \times 100\% \tag{1}$$

where C denotes its concentration of the given solution at a specific time (t) and C_0 is adsorption–desorption equilibrium conc. of solution at the time (t_0). To calculate the dye degradation apparent rate constant, Langmuir–Hinshewood's pseudo-first-order kinetic model equation was used;

$$\ln\left(C_0/C_t\right) = k_{app}t = kKt \tag{2}$$

where C is the dye concentration, k is the rate constant of the reaction, t is the degradation time, the apparent rate constant is denoted by K_{app}, and the adsorption coefficient of dye over catalyst particles is K.
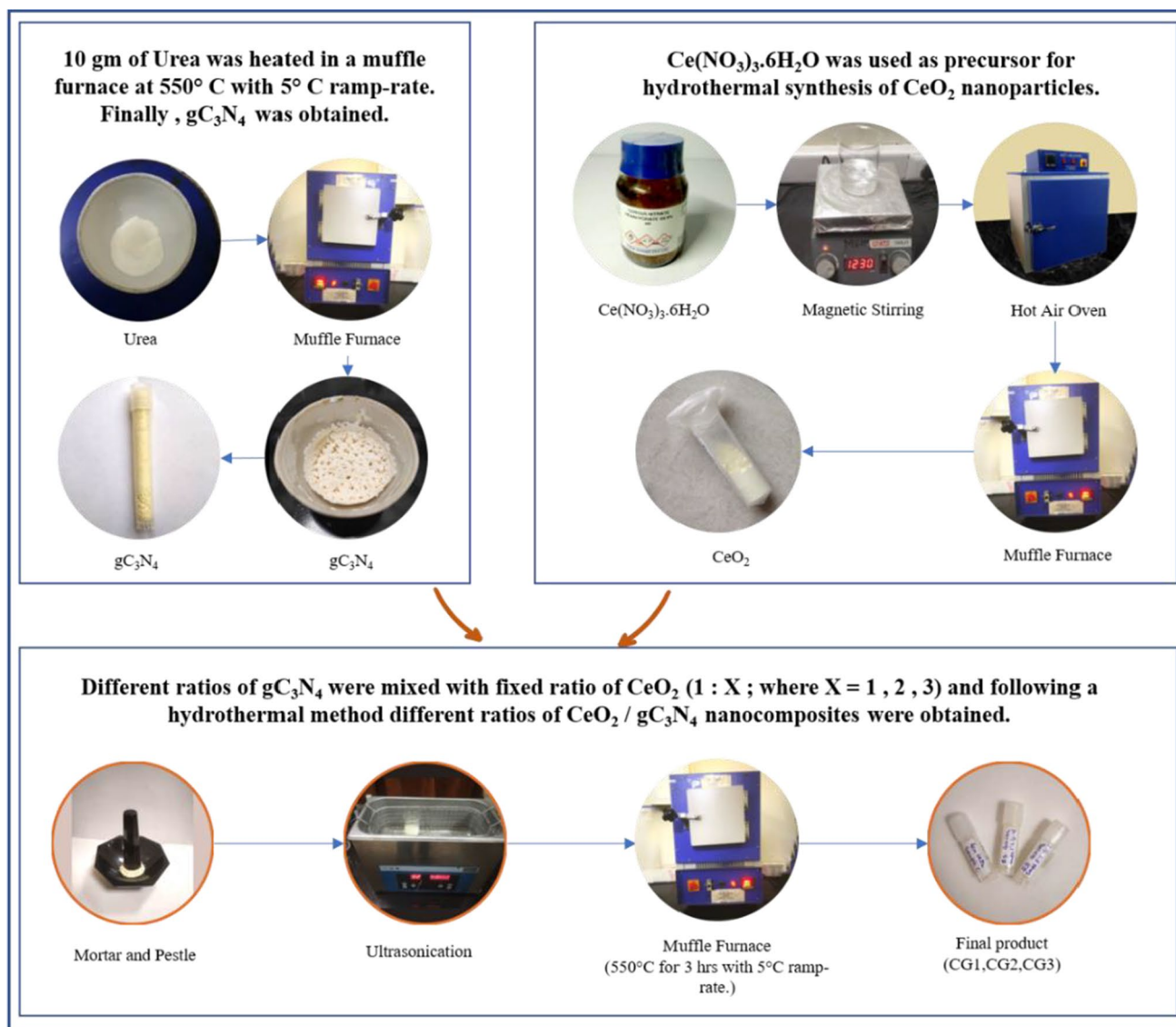
Fig. 1 Synthesis of CeO₂/GCN nanocomposites

Antibacterial activity

The Kirby-Bauer disc diffusion technique (Jorgensen and Turnidge 2009) was used to investigate antibacterial activity in prepared samples. The pathogenic strains of gram-positive bacteria, i.e., *Bacillus cereus* and *Staphylococcus aureus*, and gram-negative bacteria, i.e., *Escherichia coli* and *Salmonella abony*, were obtained from the Micro Engineering and Testing Laboratory, Sonipat. During the process, sterile nutritional agar (30 mL) media was placed and uniformly spread in a petri dish. After the agar medium was set in the plate, the bacterial suspension (0.5 mL) was dispersed over it with a spreader, followed by the formation of wells. Further, a test sample (10, 30, 50, and 70 µg/mL) was diffused into a well on an agar medium-containing plate and held under laminar air flow for 20 min. Later, plates were placed upright in an incubator for 24 h at 37 °C before the inhibitory zone was observed and calculated. All tests were repeated thrice, and the findings were stated as a mean of ± 0.01.

Results and discussion

XRD analysis

As illustrated in Fig. 2, the crystalline structure of CeO₂/GCN nanocomposites was examined by XRD (X-ray diffraction). The diffraction peaks of GCN at 28° correspond to the (002) plane, which is an interlayer stacking reflection. With
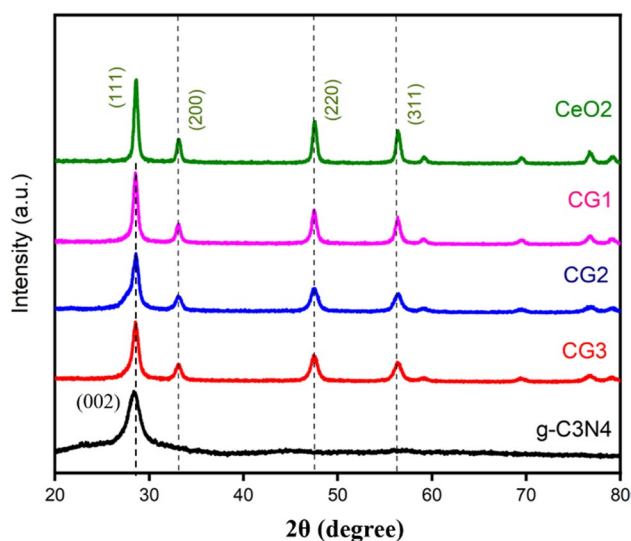
Fig. 2 XRD patterns of CeO$_2$/GCN composites

Fig. 3 FTIR spectra of CeO$_2$/GCN nanocomposites

the addition of CeO$_2$ content, diffraction peaks of CG nanocomposite series at 28°, 33.1°, 47.5°, and 56.3° developed, and their intensities grew gradually, and they were ascribed to the (111), (200), (220), and (311) planes of CeO$_2$ crystal in an order. The diffraction peak of CeO$_2$ has a significantly higher intensity compared to GCN; therefore (002) plane of GCN is not visible in the CG nanocomposite series. According to the XRD interpretation, the production of said CeO$_2$/GCN composite has a cubic and crystalline phase of CeO$_2$ and GCN, respectively, which is explicitly proven.

FTIR spectral analysis

The structure of the CeO$_2$/GCN nanocomposite was discovered by analyzing sample FTIR spectra, as shown in Fig. 3. N–H stretches caused the big peaks between 3600 and 3000 cm^{-1}, suggesting GCN may have dangling hydrogens in its C–N layers. The peaks at 1240 and 1322 cm^{-1} represent the stretching modes of vibration of C=N along with C–N heterocycles, respectively, 1408 cm^{-1}, 1563 cm^{-1}, and 1635 cm^{-1}. The peak at 808 cm^{-1} represents the s-triazine ring system's distinctive breathing. The spectra of pure CeO$_2$ display a large absorption band between 500 and 700 cm^{-1} that can be linked to the vibrational stretching of the Ce–O bond (Abbasi et al. 2012). In addition, the characteristic vibrational peaks of GCN were identified in different CeO$_2$/GCN samples, stating that the structural integrity of GCN was intact throughout the hydrothermal process.

TGA study

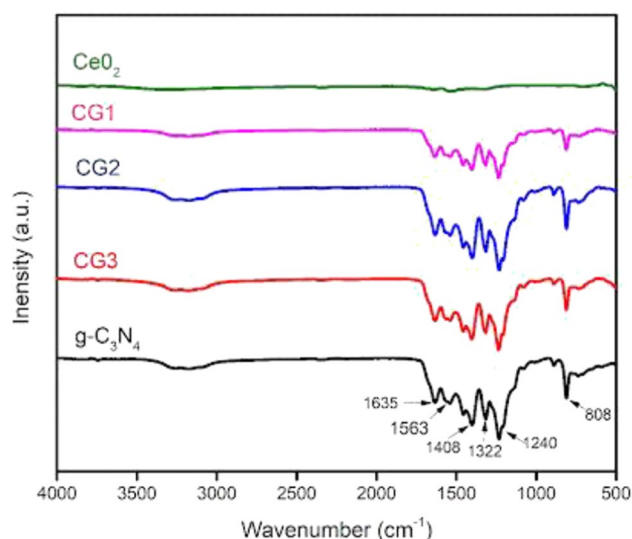Thermogravimetric testing was conducted from 35 to 800 °C at a heating rate of 10 °C/min under ideal conditions to

determine the CeO$_2$ content of the final products. Through the graphical representation (Fig. 4), it is evident that pure CeO$_2$ loses essentially no weight between 30 and 800 °C. From 550 to 680 °C, a zone of fast weight loss was seen for GCN nanoparticles, which correspond to GCN combustion. Meanwhile, a quick drop in the weight of CeO$_2$/GCN composites at temperatures of about 450 °C indicates the combustion of graphitic carbon nitride. CeO$_2$ is responsible for this outcome as it absorbs and sustains aerially reactive O$_2$, which subsequently oxidizes graphitic carbon nitride. The amount of CeO$_2$ contained in the nanocomposites was easily calculated by weighing samples on exposure to heat at around 800 °C. On close observation of the graph,
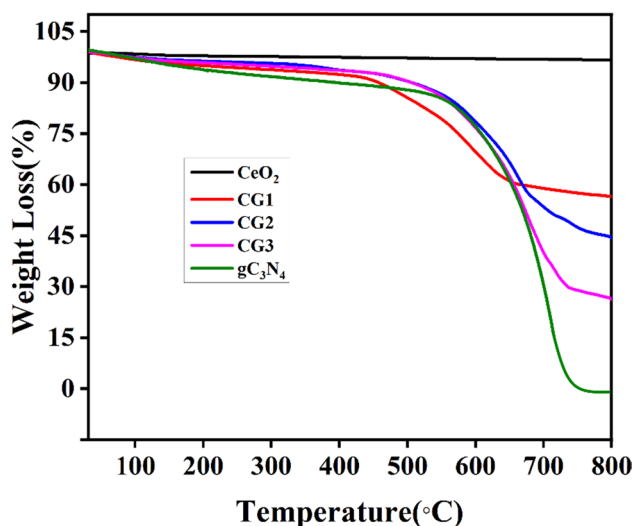

Fig. 4 TGA curves of CeO$_2$/GCN composites

the contents of CeO_2 in as-prepared nanocomposites were reported to be CG1 (26%), CG2 (44%), and CG3 (56%).

SEM morphological study

Using scanning electron microscopy (SEM), morphological and microstructural characteristics of the material were studied. In pure GCN and CG2, a unique morphology was discovered. The SEM imaging (Fig. 5a) reveals the pure layered structure and stacked-layer morphology of urea-derived GCN. In pure CeO_2 SEM images (Fig. 5b), the visible particles are observed to be aggregated and possess a crystalline phase. Figure 5c indicates that on adding CeO_2 in pure GCN, CG2 evolved into a slacked interlinked network having a mean size of 14.78 nm.

TEM analysis

In Fig. 6, it is evident that ultrafine CeO_2 has a cube structure and that the CeO_2 nanoparticles CeO_2 are bound to GCN. Figure 6 depicts the morphology of the CG2 composite material. The dark-colored particles correspond to CeO_2, whereas the gray region corresponds to GCN. CeO_2 nanoparticles with an average of 14.78 nm are found sticking to the edge and surface of the GCN. Strong contact between CeO_2 nanoparticles and GCN layers can be visualized as even after an extended ultrasonication process. The nanocomposite could not be destroyed, being essential for the electronic transmission among the desired component semiconductors.

The EDS result of the sample, shown in Fig. 7a, shows that the CG2 sample has C and O peaks along with Ce and N peaks. So, the comparison of EDS elemental data shows that the CG2 composite has Ce, C, O, and N elements, which appeared from both GCN and CeO_2 compounds. In the same way, Fig. 7b–f shows the mapping of elements of the CG2 composite as shown by the EDS testing, which once again confirms the presence of corresponding elements of C, O, N, and Ce in the CG2 nanocomposite. The analysis shows that CeO_2 particles are spread out evenly on the surfaces of
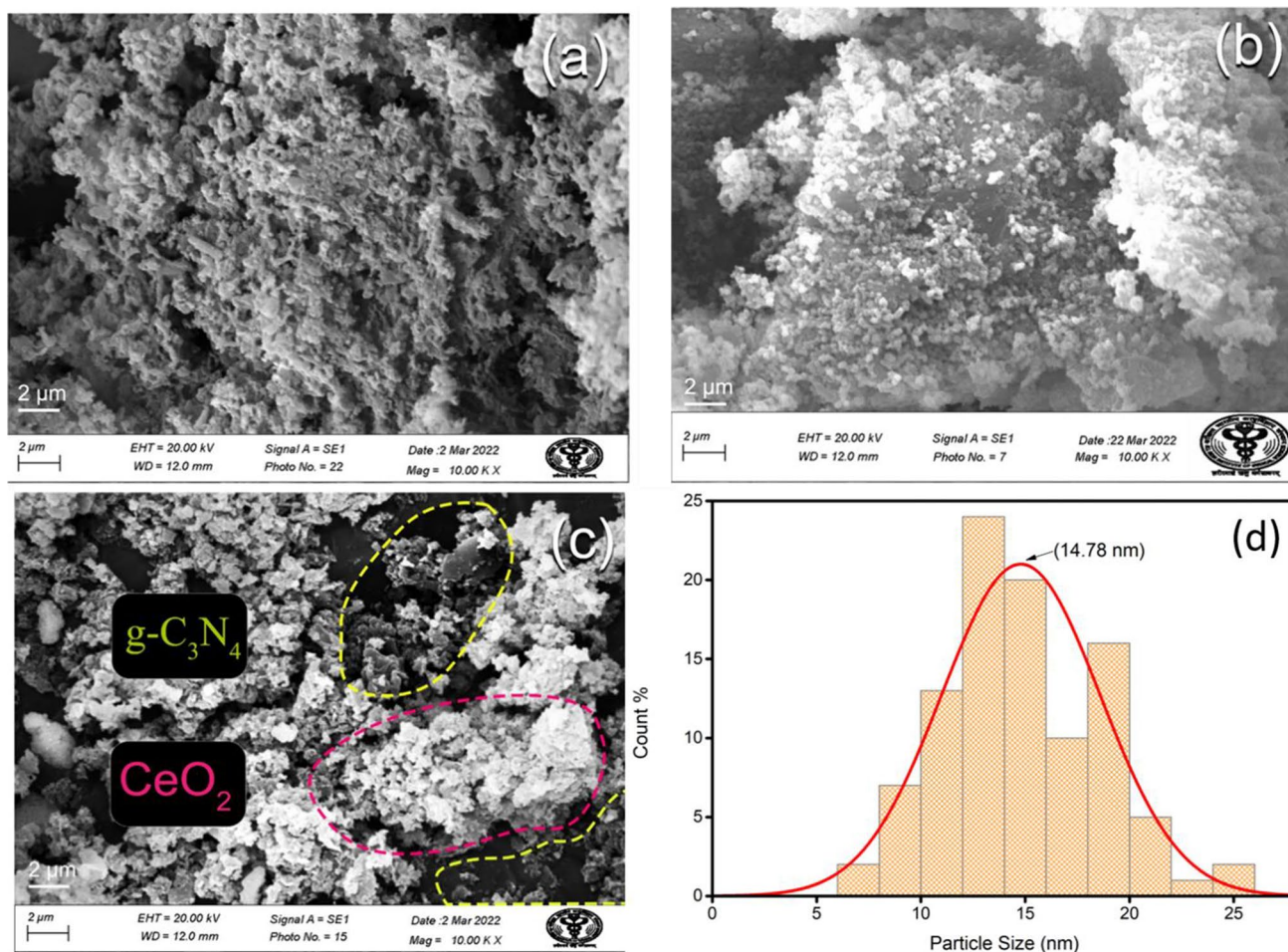

Fig. 5 The SEM images of **a** GCN, **b** CeO_2, **c** CG2 nanocomposite, and **d** average particle size
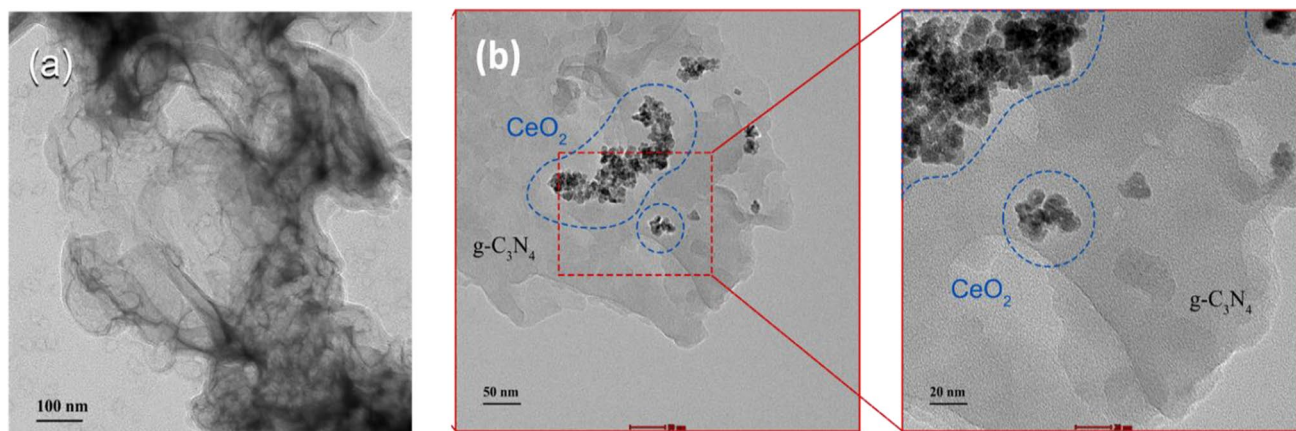
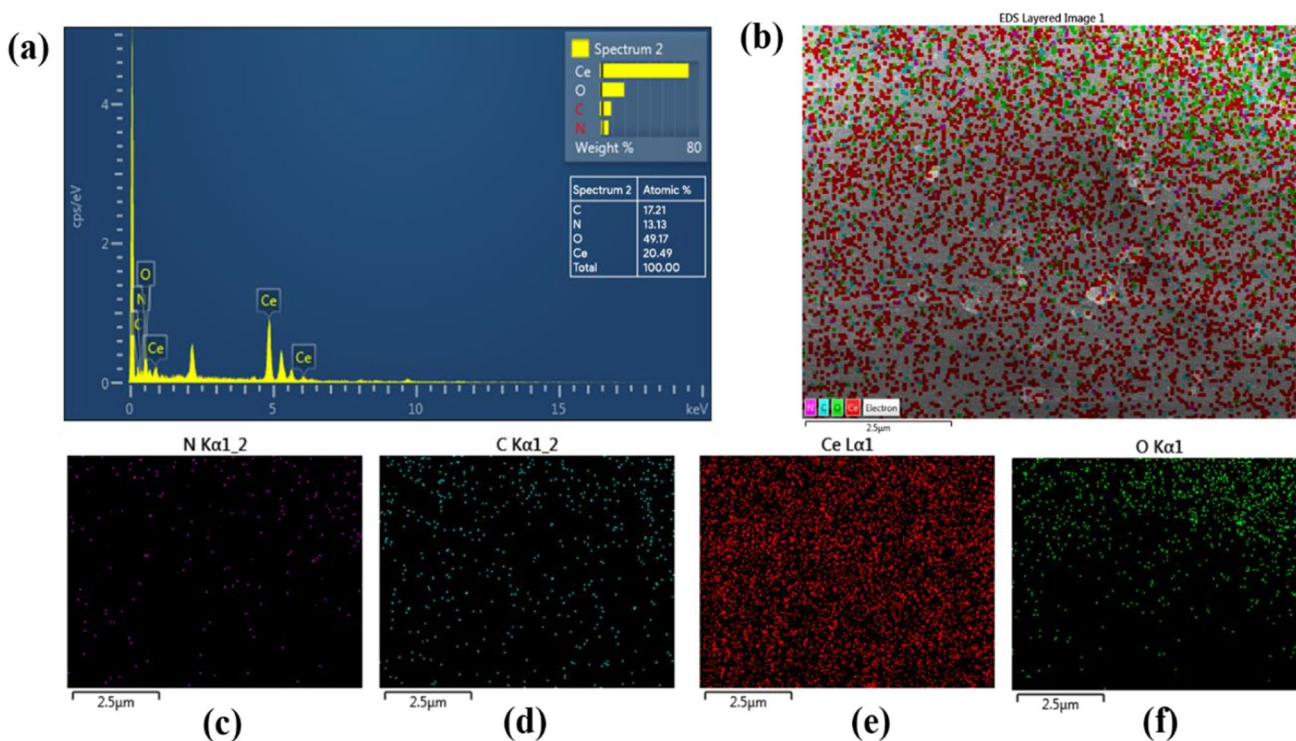**Fig. 6** TEM images of **a** GCN and **b** CG2 nanocomposite

Fig. 7 **a** EDS analysis of CG2 composite and **b–f** elemental mapping of the CG2 composite containing N, C, Ce, and O elements

the GCN layers, which supports the promising form of the CG2 nanocomposite without any visible contamination.

XPS analysis

XPS analysis was done to determine the valence states of different species. The XPS spectra of GCN and CG2 composite are shown in Fig. 8a. The finding suggests that N, O, C, and Ce are present in the CG2 nanocomposite. Figure 8b–e shows spectra with high resolution for Ce3d, O1s, C1s, and N1s. Figure 8b represents the XPS spectrum of Ce3d for CG2 composite. The major peaks of $Ce^{4+}3d^{2.5}$ and $Ce^{4+}3d^{1.5}$ are seen at 898.2 and 916.5 eV, respectively. $Ce^{3+}3d^{2.5}$ and $Ce^{3+}3d^{1.5}$ have peaks at 882.4 and 900.5 eV, respectively. Two more peaks at 907.6 and 888.8 eV are caused by the "shake-up" of $Ce^{3+}3d^{1.5}$ and $Ce^{3+}3d^{2.5}$, respectively. This spectrum is entirely compatible with a study that has already been described by (Tang et al. 2011). Figure 8c shows the XPS spectra of C1s for the composite of GCN and CG2. The C–N–C coordination has a binding energy of 288.2 eV (Yan
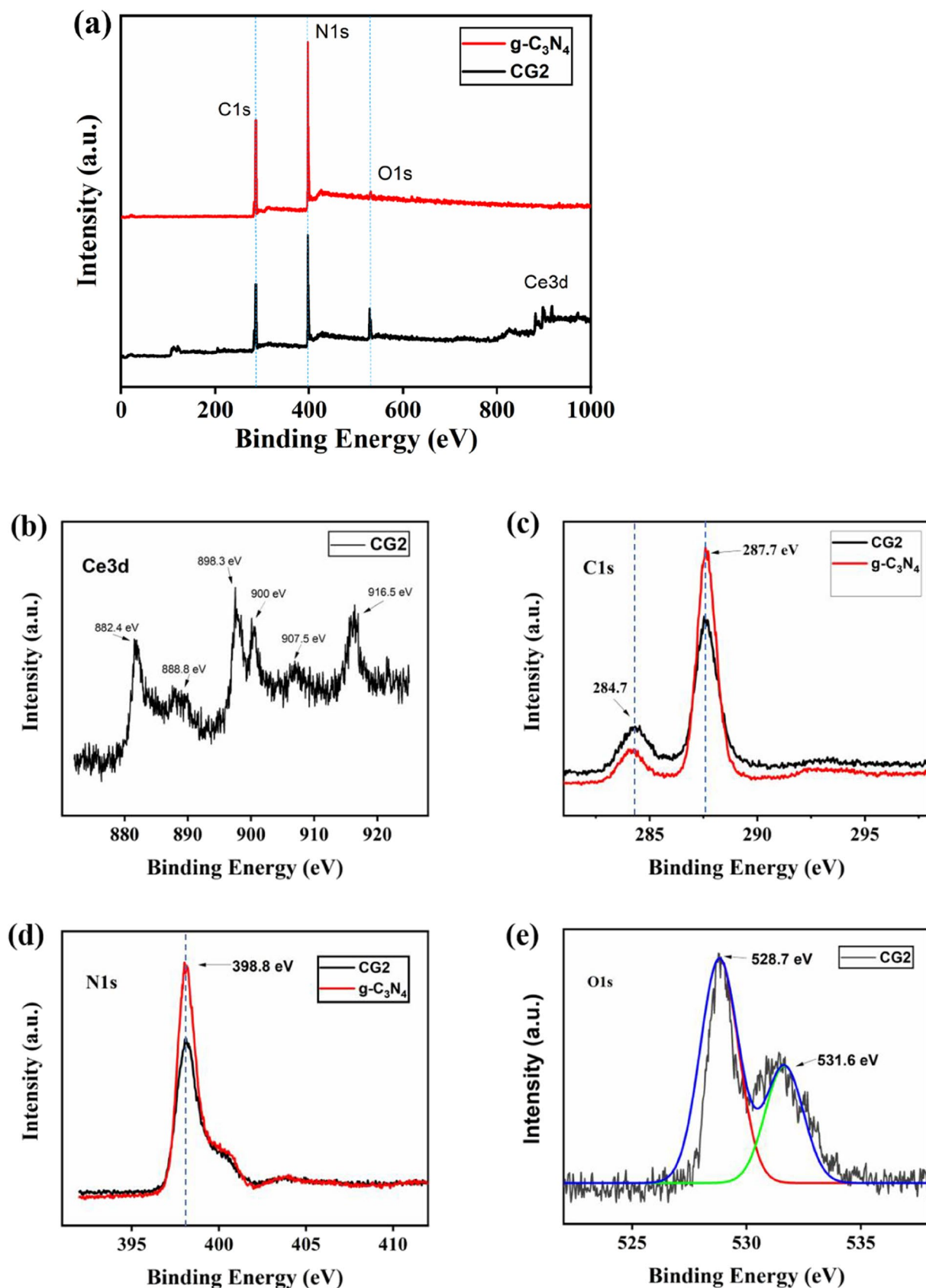
Fig. 8 **a** XPS survey spectra of GCN and CG2 composite; XPS spectra of **b** Ce3d, **c** C1s, **d** N1s, and **e** O1s

et al. 2010). The peak of C1s at 284.8 eV is due to the extra carbon present on the surface of CeO$_2$/GCN nanocomposites (Niu et al. 2012). When compared to the binding energy of N1s for GCN, it was found that CG2 nanocomposite also had a similar binding energy at 398.8 eV (Fig. 8d). This could be attributed to (C=N–C) sp^2-hybridized nitrogen (Li et al. 2009; Yan et al. 2010), which confirms the presence of sp^2-bonded GCN. The XPS spectra of O1s for the CG2 composite are shown in Fig. 8e. The asymmetric O1s profile can be represented by fitting two symmetrical peaks at 531.6 and 528.9 eV, demonstrating the presence of two different oxygen species in the material. The peak of the O1s at 528.9 eV is related to the O$_2^-$ in CeO$_2$. Another O1s peak, which is located at 531.6 eV, is connected to the –OH group or H$_2$O molecule on the surface of the CG2 composite (Ola and Mercedes Maroto-Valer 2014).

Photoluminescence

The PL spectra for GCN and CG2 nanocomposites are illustrated in Fig. 9 to study the influence of the separation efficiency of produced electron holes in the semiconductors. The major peak of the GCN sample is around 460 nm. This can be explained by the band-band PL effect, which happens when the energy of light is about the same as the band gap energy of GCN (Jia et al. 2017). The emission intensity of the CeO$_2$/GCN nanocomposites considerably dropped when CeO$_2$ nanocrystals were added, indicating that the nanocomposites had a much lower rate of recombination of photogenerated charge carriers (Huang et al. 2013). As indicated in Fig. 9(inset), the PL spectrum of CeO$_2$ nanoparticles has several strong photoluminescence peaks at 468 nm and three relatively weak peaks at 451, 482, and
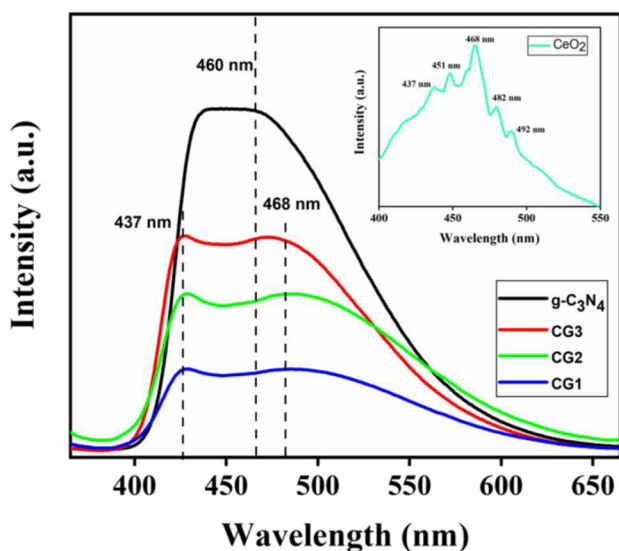
492 nm, respectively. The study found that the CeO$_2$ sample's emission bands from 400 to 500 nm are caused by the hopping between different levels of defects from the Ce-4f band to the O2p band (Sun et al. 2005). It is proposed that the numerous defects of such dislocations are responsible for the CeO$_2$ nanoparticles' strong emission at 469 nm, which is beneficial for quick oxygen transfer.

Electrochemical impedance spectroscopy (EIS)

EIS was used to investigate interfacial characteristics by measuring the frequency and resistance behavior of CeO$_2$, GCN, and their composite modified electrodes. EIS measurements were conducted in the frequency range of 10^5 to 0.1 Hz to study the electron transfer characteristic of the modified electrodes in the H$_2$SO$_4$ electrolyte solution. Figure 10a shows Nyquist plots of GCN, CeO$_2$, CG1, CG2, and CG3 electrodes, where Z″ and Z′ denote imaginary and real impedance, respectively. The higher frequency area indicates solution resistance in this case. All nanocomposite electrode materials exhibited a nearly vertical line with no semicircular zone, explaining the least charge storage circulation.

To properly understand the Nyquist plot, an electrical equivalent circuit (EEC) is fitted to experimental data. Figure 10b depicts experimental and fitting data for a CG2 sample, along with the associated simulated EEC. "Rs" stands for electrolyte or solution resistance, "Rct" refers to charge transfer resistance, and "CPE" denotes constant phase element. The non-ideal behavior of the capacitor is caused by the CPE inserted in the circuit and the "n" value. For an ideal capacitor, the value of n should be 1, which depends on the roughness and heterogeneity of the modified electrode surface and electrolytic diffusion. In this case, the value of n is getting closer to high numbers; it is 0.87 for the CG2 sample, which is close to the ideal behavior of the electrode. Table 2 shows EEC-fitted EIS data for CeO$_2$, GCN, and CG series. The solution resistance (Rs) for GCN and CeO$_2$ was discovered to be 5.83 and 7.06, respectively, which is reduced to 3.43 for the CG2 sample. The charge transfer resistance (Rct) values for GCN, CeO$_2$, CG1, CG2, and CG3 samples were 8.37, 1.38, 3.18, 1.37, and 4.18, respectively. As a result, the CG2 sample has better capacitive values than the other samples because it has the lowest Rs and Rct values with a constant phase element (CPE) of 179 mMHO. Even the CG2 n value of 0.82, which is close to one, illustrates their capacitive nature. The result suggests that the type-II heterostructured CG2 accelerated the photogenerated electron–hole pairs separation at the CeO$_2$/GCN interface, where the electrons can be efficiently transferred to CeO$_2$ (Lin et al. 2019). All results proved that the type II heterojunction of CeO$_2$/GCN is an efficient photocatalytic material for organic dye degradation.
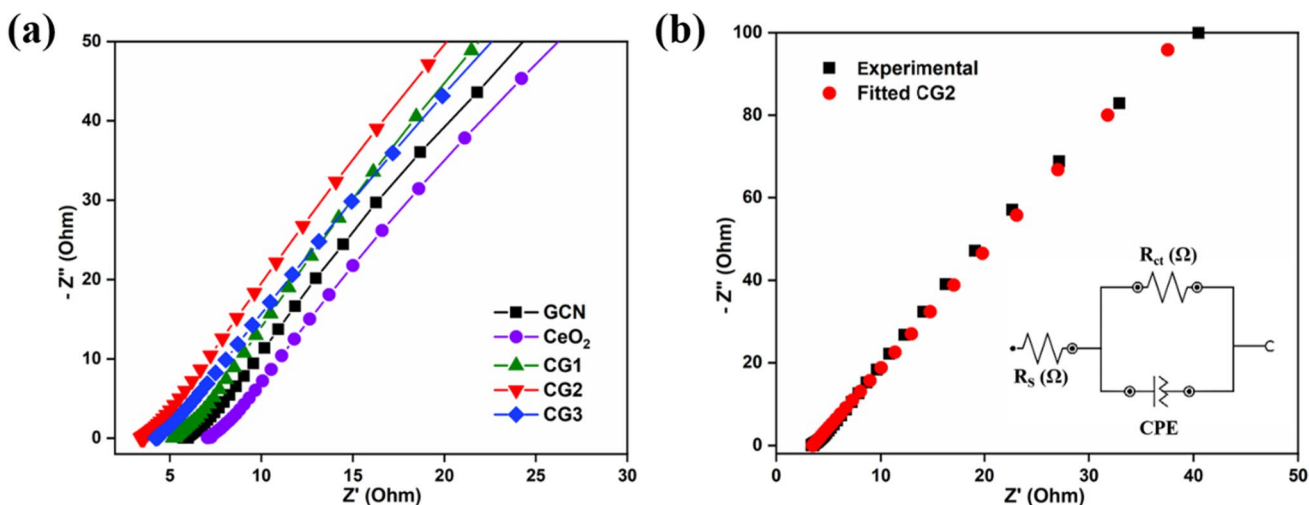

Fig. 9 PL spectra of GCN, CeO$_2$, and CG2 nanocomposites

Fig. 10 **a** Nyquist plot of pure GCN, CeO$_2$, and CG nanocomposites and **b** EEC fitted EIS data for CG2 nanocomposite

Table 2 EEC fitted data of EIS for different samples

Sample	R_S (Ω)	R_{ct} (Ω)	CPE (mMHO)	n
GCN	5.83	8.37	18.1	0.79
CeO$_2$	7.06	2.38	8.27	0.78
CG1	5.16	3.18	5.39	0.79
CG2	3.43	1.37	1.16	0.82
CG3	4.21	4.18	4.62	0.78

Cyclic voltammetry (CV)

CV is an effective and well-known electrochemical technique that is used to study both the quality and quantity of electrode materials that have been synthesized. CV of modified electrodes was measured at various scan rates in 1 M H$_2$SO$_4$ electrolyte over a potential range of 0.5 to − 0.5 V to study electroactive surface and reaction kinetics. Figure 11 shows the CVs of modified electrodes GCN, CeO$_2$, CG1, CG2, and CG3 at a scan rate of 50 mV/s in the electrolyte mentioned above. In comparison to pure CeO$_2$ and GCN, the CG nanocomposite series has the highest surface area, indicating that there is significant interaction between CeO$_2$ and GCN nanoparticles. Moreover, the peak current value of CG2 had a distinct increase with a peak potential of almost no change, indicating enhanced electrocatalytic activity (Li et al. 2015). Based on the results of the CV test, we can say that the CG2 sample has the highest surface area and a high current response at a scan rate of 50 mV/s. This indicated the increased electrocatalytic activity resulting due the smaller particle size and broader surface area, generating even more reactive sites that can help in the photodegradation of organic dyes.
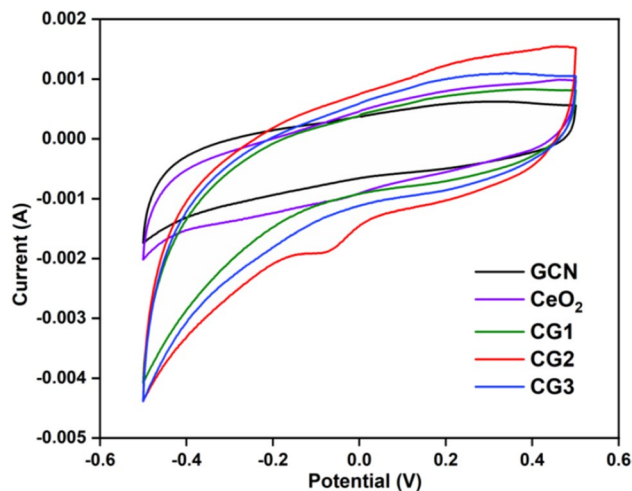

Fig. 11 CVs of pure GCN, CeO$_2$, and CG nanocomposites

UV–visible spectroscopic analysis

Figure 12a compares the UV–vis spectroscopic study of the optical absorption characteristics of samples of CeO$_2$, GCN, and CeO$_2$/GCN nanocomposites. GCN and CeO$_2$ samples absorb UV in the visible region up to 378.4 and 347.5 nm, respectively. After CeO$_2$ is combined with GCN to produce a CeO$_2$/GCN composite, the absorption remains near 412.5 nm, but the intensity increases. Such a rise in the intensity of wavelengths absorbed in the visible range is a sign that the composite is active in photocatalysis, which may prove beneficial in other photocatalytic applications. The proven photocatalytic response of the CeO$_2$/GCN composite falling under the UV–vis range is suspected to be the creation of dynamic electron–hole pairs in response to light irradiation, resulting in increased photocatalytic activity. In
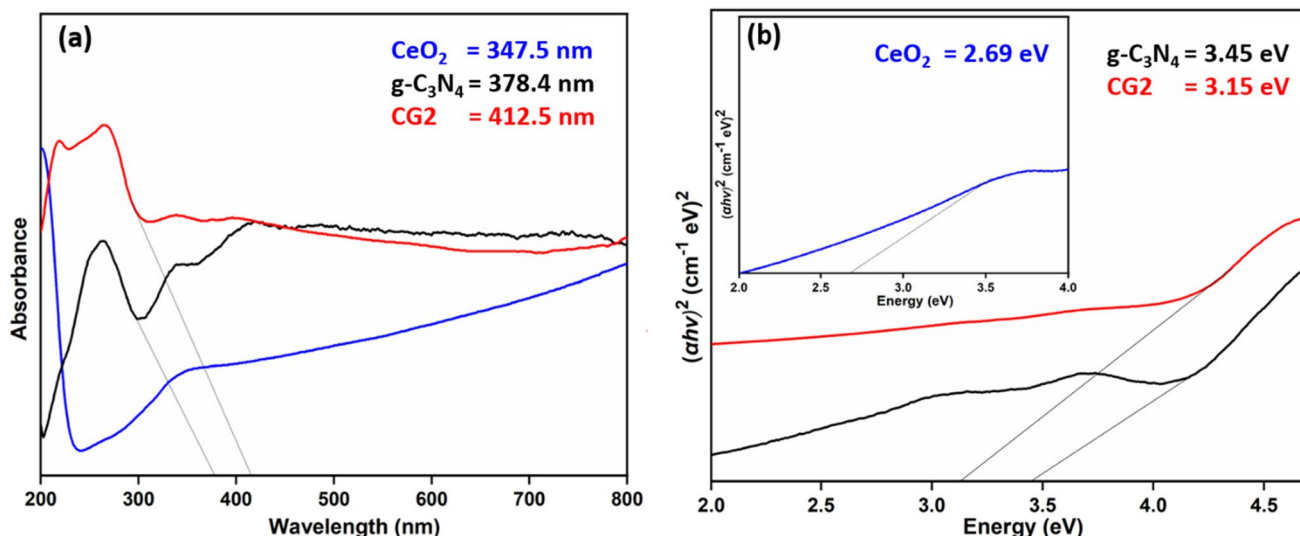
Fig. 12 **a** UV–vis absorbance spectra and **b** Tauc plot of GCN, CeO$_2$, and CG2 nanocomposite

addition, for the determination of composing samples, following Tauc's Eq. (3) was used

$$ahv = C(hv - Eg)^{1/2} \tag{3}$$

E_g is the bandgap energy, where C is the coefficient of absorption, which remains constant and unaffected by photon energy. Through Fig. 12b, we can analyze Tauc's plot with respect to the bandgap energies of the composites. The

derived bandgap energies for GCN and CeO$_2$ are 3.45 and 2.69 eV, respectively. Whereas the bandgap energy for the CeO$_2$/GCN composite is 3.14 eV, indicating that the addition of CeO$_2$ to GCN enhanced the composite's band energy gap. Since the bandgap energy of g-C$_3$N$_4$ is around 3.45 eV, along with CeO$_2$, it brings the CG2 composite's bandgap energy to 2.86 eV (Ragupathi et al. 2020). The bandgap of CeO$_2$ was calculated to be 2.69 eV. In the case of GCN, the bandgap is 3.45 eV. The bandgap of CeO$_2$ (2.69 eV) is
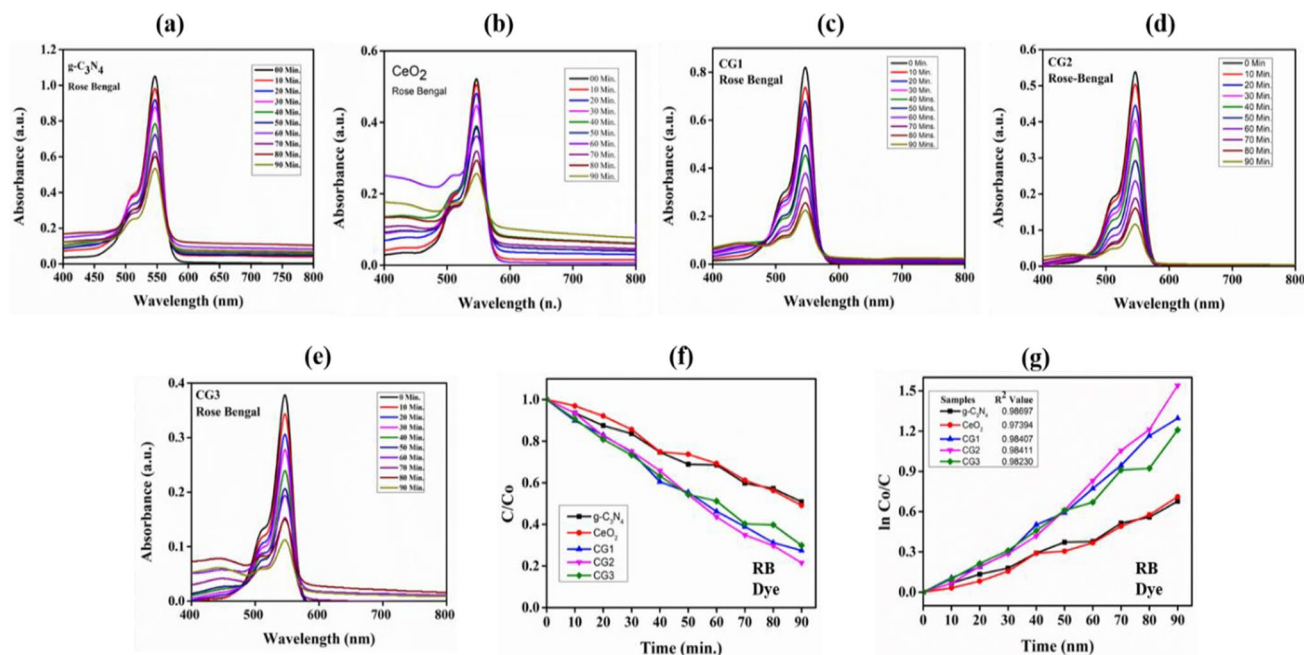

Fig. 13 **a–e** UV–visible absorbance spectra of RB dye; **f** comparison of photocatalytic activity; **g** ln(C_0/Ct) of RB dye degradation for prepared composites
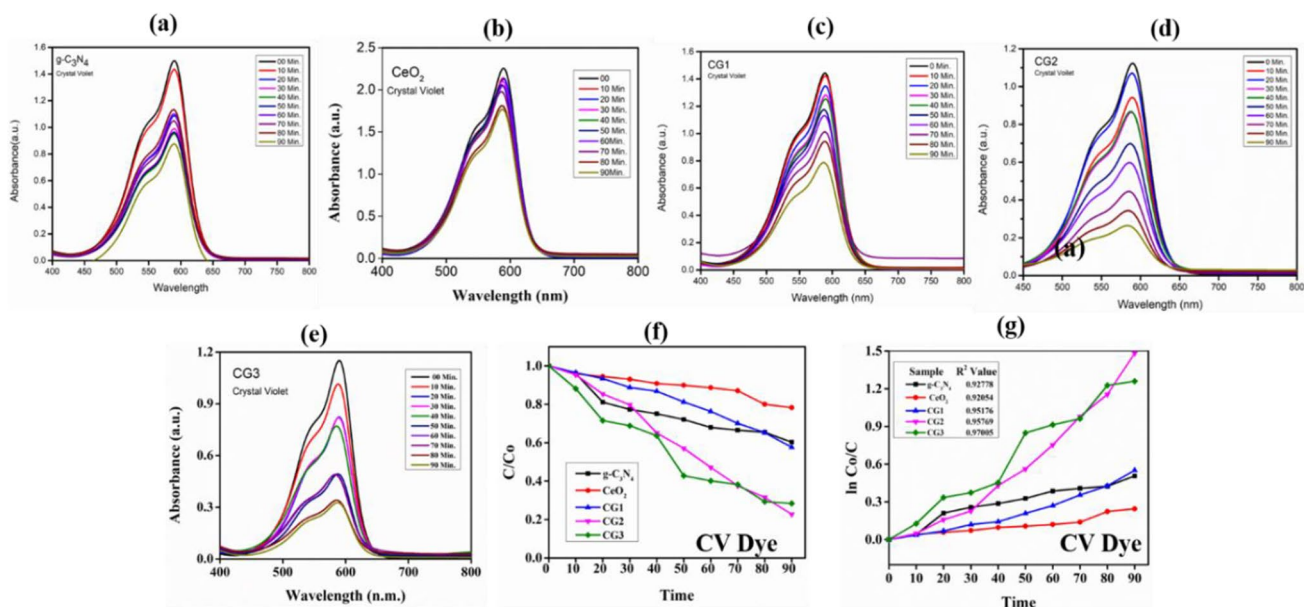
Fig. 14 **a–e** UV–visible absorbance spectra of CV dye; **f** comparison of photocatalytic activity; **g** ln(C_0/Ct) of CVdye degradation for prepared nanocomposites

less than that of GCN (3.45 eV), so the excited electrons could be transferred to the conduction band of CeO_2 from the conduction band of GCN, and the photogenerated holes of CeO_2 could transfer to GCN through the well-developed interface (Ma et al. 2019). This confirms that CeO_2/GCN has type-II heterojunctions.

The photocatalytic activity test and kinetics

Photocatalytic activity of as-prepared composites, namely GCN, CeO_2, and CG2 nanocomposite, was calculated using two distinct organic dyes, rose bengal and crystal violet (90 min). Figure 13a−e shows the photocatalytic degradation rates of GCN, CeO_2, and CeO_2/GCN nanocomposite with the RB and Fig. 14a−e for CV dyes, respectively.

In the case of rose bengal dye, the photocatalytic degradation potential of CeO_2 was found to be 51.9%.

GCN showed excellent potential and successfully degraded the RB dye up to 65%. CG1 and CG2 composites showed increasing degradation efficiency of 73.1 and 79.2%, respectively, as compared to pure GCN. The order of photocatalytic degradation of rose bengal dye is CG2 (79.2%) > CG1(73.1%) > CG3(70.2%) > GCN (65%) > CeO_2(51.9%). For CV dye, the order of photocatalytic activity is CG2 (76.7%) > CG3(71.9) > CG1(47 %) > GCN (41.6%) > CeO_2 (22.7%). In the case of CG3, a decreased photodegradation can be seen, which could be a result of the existence of surplus defects within the GCN phase of CG3 nanocomposite acting as an e^--h^+ recombination site and thus suppressing the transfer frequency of photo-induced charges, CG2 outperformed and exhibited the maximum value for the apparent rate constant, leading to an increase of 2.3 times for RB dye and 3.1 times for CV dye as compared to pure GCN, as shown in Tables 3 and

Table 3 The degradation efficiency, R^2 value, and apparent rate constant for composites

S. no	Sample	Crystal violet dye			Rose bengal dye		
		Degradation efficiency	R^2	Apparent rate constant (k) (min^{-1})	Degradation efficiency	R^2	Apparent rate constant (k) (min^{-1})
1	g-C_3N_4	41.60%	0.92778	0.00525	65%	0.98697	0.00734
2	CeO_2	22.70%	0.92054	0.00245	51.9%	0.97394	0.00782
3	CG1	47%	0.95176	0.00585	73.1%	0.98407	0.01478
4	CG2	76.70%	0.95769	0.016331	79.2%	0.98411	0.01697
5	CG3	71.90%	0.97005	0.01466	70.2%	0.9823	0.01295

Table 4 Comparison of dye degradation results from previously published works

Dye	Catalyst used	Illumination source	Degradation efficiency (%)	Time (Min)	Reference
Methylene blue	Ag/g-C$_3$N$_4$	300 W Xe lamp	58%	300	(Malik et al. 2015)
Methylene blue	MnTiO$_3$	Sunlight	75%	240	(Alkaykh et al. 2020)
Rose bengal	Ag/CeO$_2$	Sunlight	96%	180	(Murugadoss et al. 2021)
Rose bengal	CeO$_2$/GCN	400 W Xe lamp	79.2%	90	This work
Crystal violet	g-C$_3$N$_4$	200 W XE lamp	51	120	(Rattan Paul and Nehra 2021b)
Crystal violet	CeO$_2$/GCN	400 W Xe lamp	76.7	90	This work
Xylenol orange	TiO$_2$	UV lamp (7 W)	70	175	(Iliev et al. 2004)

4 shows the comparison of dye degradation results from previously reported works.

Figure 15 shows the analysis of the reusability and stability of CG2 nanocomposite. At the end of each experiment, the catalyst was collected and used again in the next cycle. For each dye, the same process was done a total of five times in a cycle. Starting with 0.01 g of catalyst, a dye solution containing 10 mg/L was added to 100 mL of water. In every experiment, the rate of degradation of the catalyst was found to be stable, with a slight drop-in activity that could be caused by the loss of catalyst during the recollection process. The cycling test shows that CG2 nanocomposite is stable enough to be used for the photodegradation of different organic dyes.
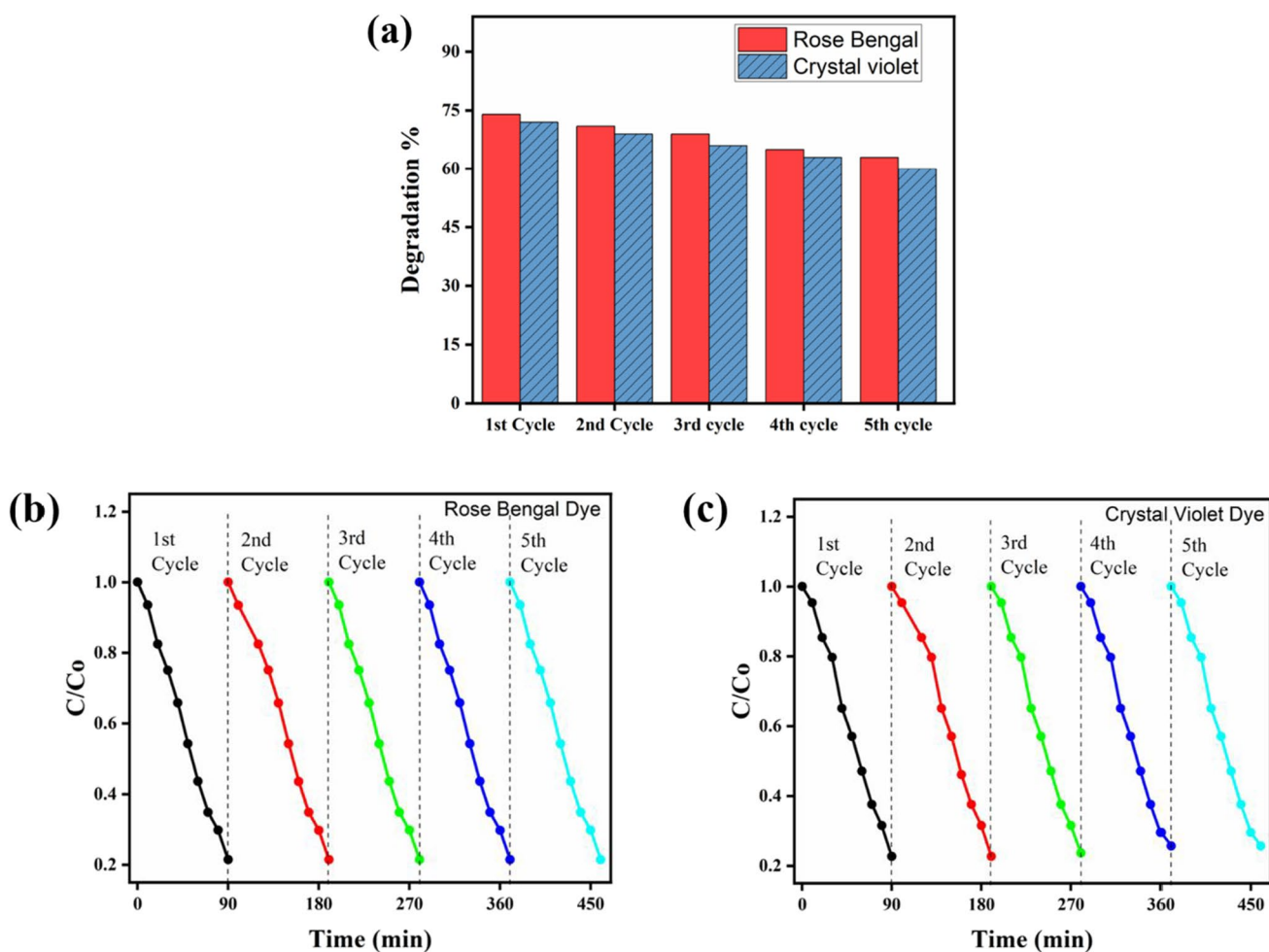

Fig. 15 **a** Recyclability experiment of the photocatalytic degradation of dyes using CG2 nanocomposite and **b** comparison of photocatalytic degradation of 5 cycles using CG2 nanocomposite
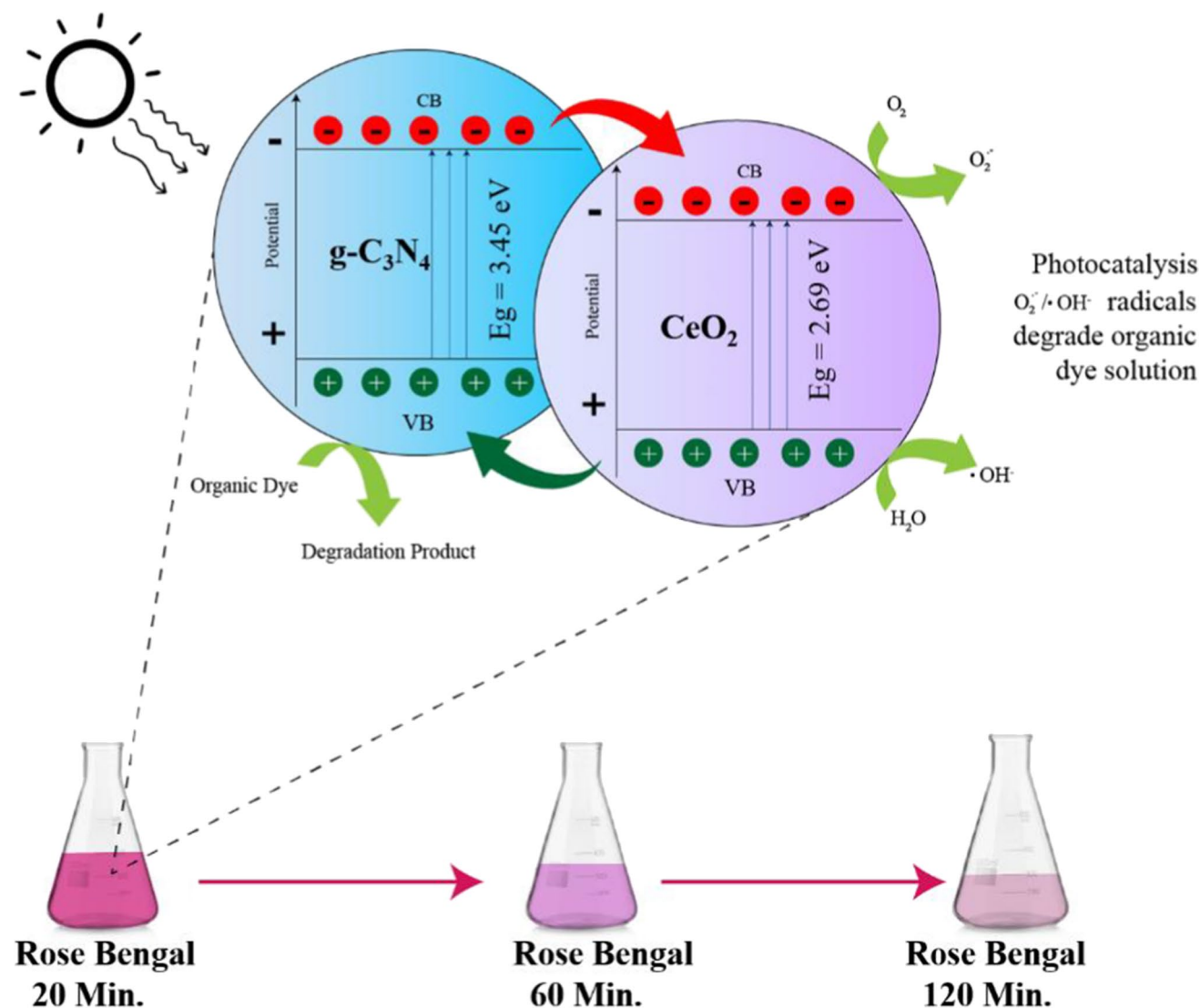
Fig. 16 Mechanism of photocatalytic degradation

Proposed mechanism for photocatalytic study

In this study, the photocatalytic performance of a stable CeO_2/GCN nanocomposite was studied and compared to nanoparticles of CeO_2 and GCN under visible light via photocatalytic reaction. The research revealed the formation of a strong adsorption intermediate by CeO_2/GCN composite that, in subsequent stages, contributed to improved photocatalytic degradation. In comparison with GCN, the adsorption of dye molecules on the surface of CG2 composite was largely due to the high surface area of CG2 composite and the $\pi - \pi$ stacking between GCN and dye (Wang et al. 2011), suggesting a good supplement for the high photocatalytic activity of the CeO_2/GCN composite. Both CeO_2 and GCN could be excited under visible light irradiation and generate photoinduced e − and

h + . The formation of CeO_2/GCN type-II heterostructure provides an internal electric field, leading to the migration of h + transfer from the VB of CeO_2 to that of GCN, whereas e − from the CB of GCN to that of CeO_2, revealing the type-II charge transfer process (Ma et al. 2019). In the case of the CeO_2/GCN composite, it is speculated that the observed photocatalytic activity is a result of the participation of certain conduction band electrons in a reaction, including adsorbed oxygen, to form superoxide radicals ($\bullet O_2$). This involvement of conduction band electrons produces holes in the valence band, which react against adsorbed water or OH molecules creating reactive hydroxyl radicals ($\bullet OH$). In the later steps, generated superoxide ($\bullet O_2$) and hydroxyl radical ($\bullet OH$) react with organic dyes (RB and CV dyes) and facilitate their degradation. Also, the catalyst may neutralize unnecessary
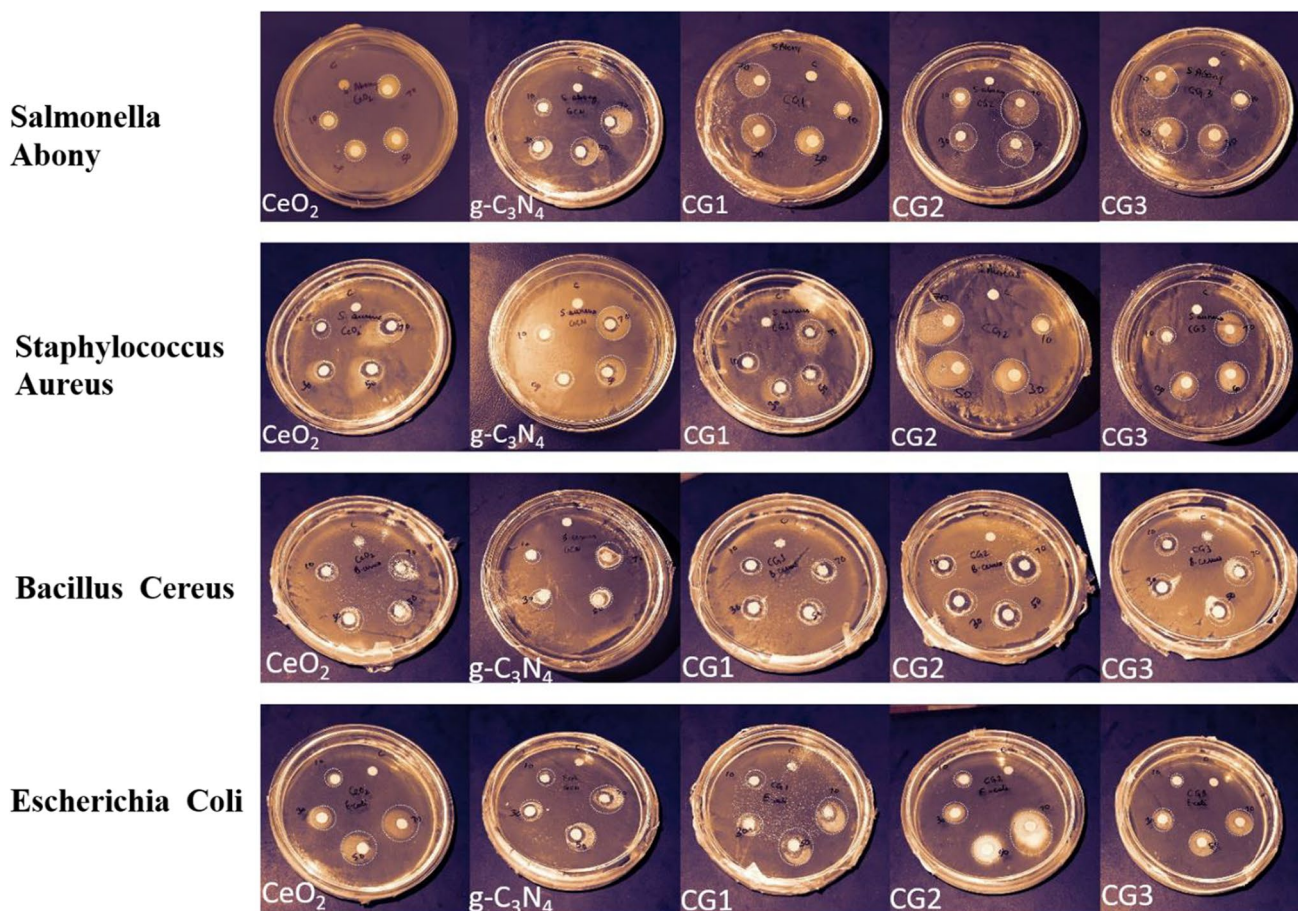
Fig. 17 Inhibition zones against *S. abony*, *S. aureus*, *B. cerrous*, and *E. coli* bacteria

superoxide ($\bullet O_2$) and hydroxyl radical ($\bullet OH$), allowing simultaneous oxidation and reduction events to proceed at the photocatalyst's surface. Figure 16 shows a possible photodegradation mechanism for CeO_2/GCN nanocomposites.

The antibacterial analysis

The result of the antibacterial study of the nanocomposites is shown in Figs. 17 and 18 and Tables 5 and 6. The obtained results signify that the zone of inhibition for the nanocomposites has changed. Figure 18 shows that the antibacterial activity of all pathogenic bacteria improved when the concentration of the material increased from 10 to 70 µg/mL. The CG2 nanoparticles at 70 µg/mL concentration generated a maximum inhibition zone of 19.9 ± 0.5 µg/mL against *E. coli*, 18.9 ± 0.5 µg/mL against *S. aureus*, 18 ± 0.5 µg/mL against *S. abony*, and $16 \pm$ µg/mL against *B. cerrous*. When GCN is used as a photocatalyst, it could make reactive oxygen species. These could disrupt the cell activity of microorganisms that come into contact with them, making it harder for them to grow and

multiply (Sun et al. 2017). The CG nanocomposite series outperformed GCN and CeO_2 in terms of antibacterial potential, which may be attributable to their superior surface area and lower optical band gap. Due to their smaller size, CG2 nanoparticles are more effective than bulk nanoparticles and enable quicker adsorption of pathogens.

Such findings with metal oxide-polymer nanocomposites have previously been reported for *S. aureus* and *E. coli* bacteria, but our study also included *S. abony* and *B. cerrous* (Kannan and Sundrarajan 2014). Table 7 compares the antibacterial activity of previously published polymer-metal oxide nanocomposites to CG nanocomposites against certain typically growing gram-negative and gram-positive bacteria.

Mechanism of antibacterial activity

Several mechanisms for metal oxide nanoparticle antibacterial activity have been reported (Kannan and Sundrarajan 2014; Arumugam et al. 2015; Reddy Yadav et al. 2016). In general, photocatalysts in the presence of dissolved oxygen can produce free radicals such as $O_2\bullet-$, $\bullet OH$, etc. This will induce
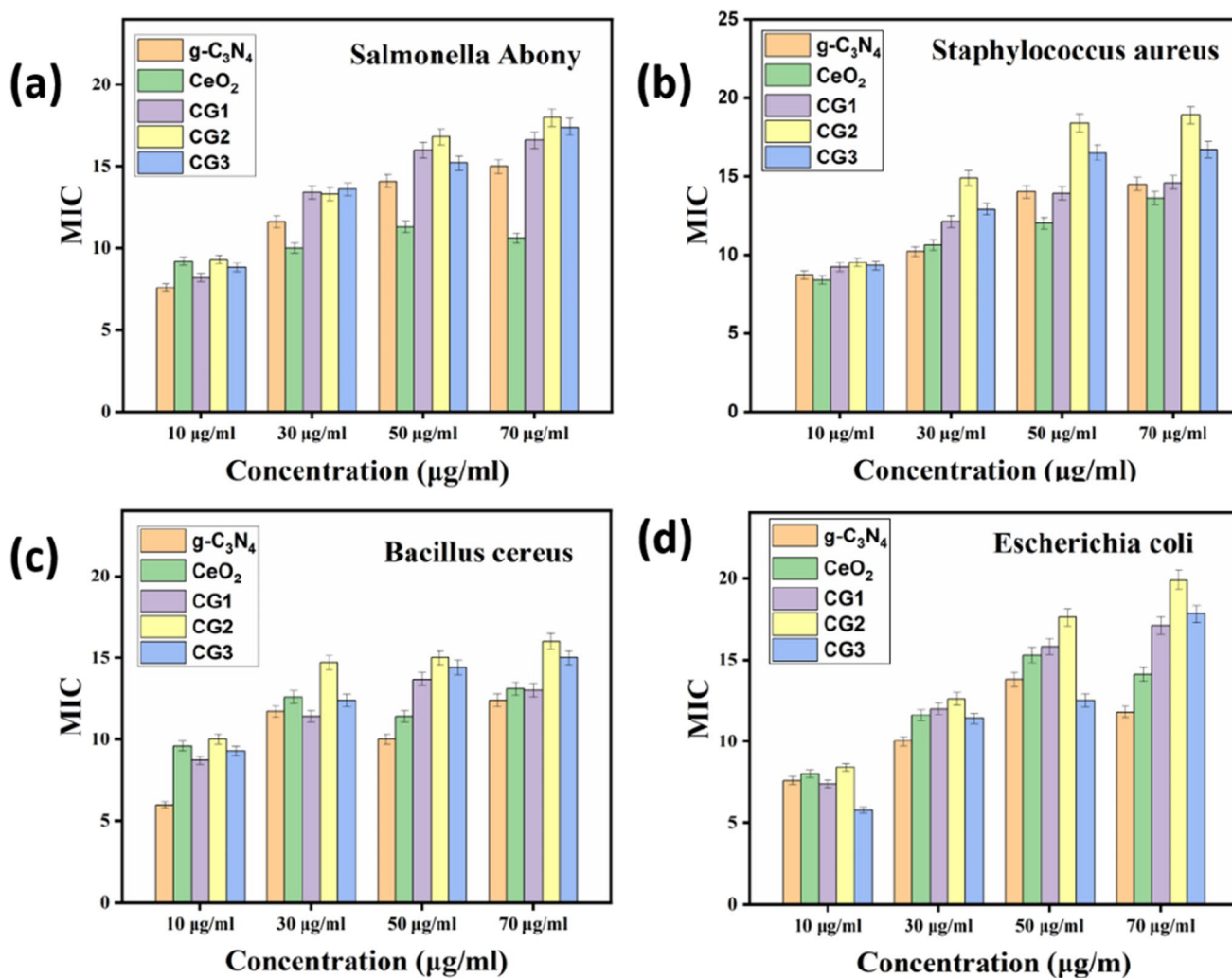
Fig. 18 Comparative inhibition zones of nanocomposites against **a** *S. abony*, **b** *S. aureus*, **c** *B. cerrous*, and **d** *E. coli* bacteria

interruptions in normal microbial cell multiplication capacity due to bacterial cell wall breakdown, inhibition of nucleic acid synthesis, cellular membrane permittivity, and enzyme action. Excessive free radical generation can harm membrane lipids, resulting in membrane collapse and mitochondrial failure or DNA damage, which can lead to bacterial cell death (Panchal et al. 2019).

Conclusion

Novel CeO_2/GCN nanocomposites were prepared successfully via a simple and facile hydrothermal process and characterized. XRD patterns showed that crystalline phase structures of CeO_2 and GCN remained unchanged after the synthesis process. SEM and TEM examined the morphology

Table 5 Diameter (mm) of zone of inhibition of Gram-positive bacteria

Gram-positive bacteria (diameter (mm) of zone of inhibition)										
	S. aureas					*B. cerrous*				
Conc	GCN	CeO_2	C1	C2	C3	GCN	CeO_2	C1	C2	C3
10 μg/mL	8.7±0.2	8.4±0.2	9.2±0.2	9.5±0.2	9.3±0.2	06±0.1	9.6±0.2	8.7±0.2	10±0.3	9.3±0.2
30 μg/mL	10.2±0.3	10.6±0.3	12.1±0.3	14.9±0.4	12.9±0.3	11.7±0.3	12.6±0.3	11.4±0.3	14.7±0.4	12.4±0.3
50 μg/mL	14±0.4	12±0.3	13.9±0.4	18.4±0.5	16.5±0.4	10±0.3	11.4±0.3	13.7±0.4	15±0.4	14.4±0.4
70 μg/mL	14.5±0.4	13.6±0.4	14.6±0.4	18.9±0.5	16.7±0.5	12.4±03	13.1±0.3	13±0.4	16±0.4	15±0.4

Table 6 Diameter (mm) of zone of inhibition of Gram-positive bacteria

Gram-negative bacteria (diameter (mm) of zone of inhibition)

Conc	*S. abony*					*E. coli*				
	GCN	CeO_2	C1	C2	C3	GCN	CeO_2	C1	C2	C3
10 µg/mL	7.6 ± 0.2	9.2 ± 0.2	8.2 ± 0.2	9.3 ± 0.2	8.8 ± 0.2	7.6 ± 0.2	8 ± 0.2	7.4 ± 0.2	8.4 ± 0.2	5.8 ± 0.1
30 µg/mL	11.6 ± 0.3	10 ± 0.3	13.4 ± 0.4	13.3 ± 0.4	13.6 ± 0.4	10 ± 0.3	11.6 ± 0.3	12 ± 0.3	12.6 ± 0.3	11.4 ± 0.3
50 µg/mL	14.1 ± 0.4	11.3 ± 0.3	16 ± 0.4	16.8 ± 0.5	15.2 ± 0.4	13.8 ± 0.4	15.3 ± 0.4	15.8 ± 0.4	17.6 ± 0.5	12.5 ± 0.3
70 µg/mL	15 ± 0.4	10.6 ± 0.3	16.6 ± 0.4	18 ± 0.5	17.4 ± 0.5	11.8 ± 0.3	14.1 ± 0.4	17.1 ± 0.5	19.9 ± 0.5	17.8 ± 0.5

Table 7 Comparison of antimicrobial efficiency of the present work with previously reported nanocomposites

Nanocomposites	Conc	Gram-positive bacteria		Gram-negative bacteria		References
		S. aureas	*B. cerrous*	*S. abony*	*E. coli*	
CeO_2/GO	50 µg/mL	8.3 mm	-	---	6.1	(Sharma et al. 2020)
CeO_2/Gd	2 mol%	15 mm	13 mm	–	13 mm	(Khadar et al. 2017)
g-C_3N_4/Cr-ZnO	50 µg/mL	19 mm	–	–	15 mm	(Qamar et al. 2020)
ZnO/g-C_3N_4	100 µg/mL	18 mm	–	---	14 mm	(Sher et al. 2021)
CeO_2/GCN	75 µg/mL	18.9 mm	16.04 mm	18.05 mm	19.9 mm	This Work

of nanocomposites, whereas UV–vis and XPS analysis stated that the obtained CeO_2/GCN composites were type-II heterostructured photocatalysts. Photoluminescence and electrochemical analysis showed the smooth transfer and high separation of photogenerated electron–hole pairs at the heterojunction interfaces between the GCN and CeO_2. The obtained results proved that CG2 nanocomposite exhibits optimal photocatalytic performance. The rate constant of the CG2 photocatalyst for CV dye was 6.6 times and 3.1 times as compared to CeO_2 and GCN, respectively, and for RB dye, the rate constant of the CG2 photocatalyst was 2.1 times and 2.3 times to that of CeO_2 and GCN, respectively. The notable and enhanced activity of the CeO_2/GCN composite happened due to the synergistic effect among the interface of GCN with that of CeO_2, leading to the suitable band positions and significant adsorption ability for CeO_2/GCN composites. The antibacterial analysis showed that CG2 nanocomposite also inhibited severe and commonly occurring pathogenic bacteria, including *E. coli*, *S. aureus*, *S. abony*, and *B. cerrous*, with good inhibition efficiency. Thus, it can be confirmed that CeO_2/GCN composites have the potential to be a sustainable photocatalyst for bacterial disinfection and organic pollutant removal applications. This refining and formation of CeO_2/GCN composites may provide a platform for the creation of an advanced generation of photocatalytic substances, which may have distinct and more promising features.

Data availability The data are available on request.

Materials availability The data are available on request.

Declarations

Ethical approval For this type of study formal consent is not required.

Consent to participate Not applicable.

Consent for publication Not applicable.

Conflict of interest The authors declare no competing interests.

References

Abbasi Z, Haghighi M, Fatehifar E, Rahemi N (2012) Comparative synthesis and physicochemical characterization of $CeO2$

nanopowder via redox reaction, precipitation and sol–gel methods used for total oxidation of toluene. Asia-Pacific J Chem Eng 7:868–876. https://doi.org/10.1002/APJ.652

Alkaykh S, Mbarek A, Ali-Shattle EE (2020) Photocatalytic degradation of methylene blue dye in aqueous solution by MnTiO3 nanoparticles under sunlight irradiation. Heliyon 6:e03663. https://doi.org/10.1016/J.HELIYON.2020.E03663

Arumugam A, Karthikeyan C, Haja Hameed AS et al (2015) Synthesis of cerium oxide nanoparticles using Gloriosa superba L. leaf extract and their structural, optical and antibacterial properties. Mater Sci Eng C Mater Biol Appl 49:408–415. https://doi.org/10.1016/J.MSEC.2015.01.042

Channei D, Inceesungvorn B, Wetchakun N et al (2014) (2014) Photocatalytic degradation of methyl orange by CeO2 and Fe–doped CeO2 films under visible light irradiation. Sci Reports 41(4):1–7. https://doi.org/10.1038/srep05757

Dette C, Pérez-Osorio MA, Kley CS et al (2014) TiO2 anatase with a bandgap in the visible region. Nano Lett 14:6533–6538. https://doi.org/10.1021/NL503131S/SUPPL_FILE/NL503131S_SI_001.PDF

Huang L, Li Y, Xu H et al (2013) Synthesis and characterization of CeO2/g-C3N 4 composites with enhanced visible-light photocatatalytic activity. RSC Adv 3:22269–22279. https://doi.org/10.1039/c3ra42712a

Iliev V, Tomova D, Bilyarska L, Petrov L (2004) Photooxidation of xylenol orange in the presence of palladium-modified TiO2 catalysts. Catal Commun 5:759–763. https://doi.org/10.1016/J.CATCOM.2004.09.005

Jia T, Li J, Long F, et al (2017) Ultrathin g-C3N4 nanosheet-modified biocl hierarchical flower-like plate heterostructure with enhanced photostability and photocatalytic performance. Crystals 7.https://doi.org/10.3390/CRYST7090266

Jorgensen JH, Turnidge JD (2009) Susceptibility test methods: Dilution and disk diffusion methods. Manual of Clinical Microbiology, pp 1253–1273. https://doi.org/10.1128/9781555817381.ch71

Kannan SK, Sundrarajan M (2014) A green approach for the synthesis of a cerium oxide nanoparticle: characterization and antibacterial activity 13. https://doi.org/10.1142/S0219581X14500185

Kesarla MK, Fuentez-Torres MO, Alcudia-Ramos MA et al (2019) Synthesis of g-C3N4/N-doped CeO2 composite for photocatalytic degradation of an herbicide. J Mater Res Technol 8:1628–1635. https://doi.org/10.1016/j.jmrt.2018.11.008

Khadar YAS, Balamurugan A, Devarajan VP, Subramanian R (2017) Hydrothermal synthesis of gadolinium (Gd) doped cerium oxide (CeO2) nanoparticles: characterization and antibacterial activity. Orient J Chem 33:2405–2411. https://doi.org/10.13005/OJC/330533

Khobragade R, Roškarič M, Žerjav G et al (2021) Exploring the effect of morphology and surface properties of nanoshaped Pd/CeO2 catalysts on CO2 hydrogenation to methanol. Appl Catal A Gen 627:118394. https://doi.org/10.1016/J.APCATA.2021.118394

Li L, Wang H, Zou L, Wang X (2015) Controllable synthesis, photocatalytic and electrocatalytic properties of CeO2 nanocrystals. RSC Adv 5:41506–41512. https://doi.org/10.1039/C5RA06213F

Li M, Zhang L, Wu M et al (2016) Mesostructured CeO2/g-C3N4 nanocomposites: remarkably enhanced photocatalytic activity for CO2 reduction by mutual component activations. Nano Energy 19:145–155. https://doi.org/10.1016/J.NANOEN.2015.11.010

Li X, Zhang J, Shen L et al (2009) Preparation and characterization of graphitic carbon nitride through pyrolysis of melamine. Appl Phys A Mater Sci Process 94:387–392. https://doi.org/10.1007/S00339-008-4816-4

Lin J, Liu Y, Liu Y et al (2019) SnS 2 nanosheets/H-TiO 2 nanotube arrays as a type II heterojunctioned photoanode for photoelectrochemical water splitting. Chemsuschem 12:961–967. https://doi.org/10.1002/CSSC.201802691

Ma R, Zhang S, Li L et al (2019) Enhanced visible-light-induced photoactivity of type-II CeO2/g-C3N4 nanosheet toward organic pollutants degradation. ACS Sustain Chem Eng 7:9699–9708. https://doi.org/10.1021/acssuschemeng.9b01477

Malik R, Tomer V, Duhan S et al (2015) Effect of annealing temperature on the photocatalytic performance of SnO 2 nanoflowers towards degradation of rhodamine B. Adv Sci Eng Med 7:448–456. https://doi.org/10.1166/ASEM.2015.1715

Mittal A, Mari B, Sharma S et al (2019) Non-metal modified TiO 2: a step towards visible light photocatalysis. J Mater Sci Mater Electron 30:3186–3207. https://doi.org/10.1007/S10854-018-00651-9/TABLES/7

Murugadoss G, Kumar DD, Kumar MR et al (2021) Silver decorated CeO2 nanoparticles for rapid photocatalytic degradation of textile rose bengal dye. Sci Reports 111(11):1–13. https://doi.org/10.1038/s41598-020-79993-6

Niu P, Liu G, Cheng HM (2012) Nitrogen vacancy-promoted photocatalytic activity of graphitic carbon nitride. J Phys Chem C 116:11013–11018. https://doi.org/10.1021/JP301026Y/ASSET/IMAGES/MEDIUM/JP-2012-01026Y_0011.GIF

Ola O, Mercedes Maroto-Valer M (2014) Copper based TiO 2 honeycomb monoliths for CO 2 photoreduction. Catal Sci Technol 4:1631–1637. https://doi.org/10.1039/C3CY00991B

Ong WJ, Tan LL, Ng YH et al (2016) Graphitic carbon nitride (g-C3N4)-based photocatalysts for artificial photosynthesis and environmental remediation: are we a step closer to achieving sustainability? Chem Rev 116:7159–7329. https://doi.org/10.1021/ACS.CHEMREV.6B00075/ASSET/IMAGES/MEDIUM/CR-2016-00075J_0172.GIF

Panchal P, Paul DR, Sharma A, et al (2019) Phytoextract mediated ZnO/MgO nanocomposites for photocatalytic and antibacterial activities. J Photochem Photobiol A Chem 385.https://doi.org/10.1016/J.JPHOTOCHEM.2019.112049

Paul DR, Sharma R, Panchal P et al (2019) Silver doped graphitic carbon nitride for the enhanced photocatalytic activity towards organic dyes. J Nanosci Nanotechnol 19:5241–5248. https://doi.org/10.1166/JNN.2019.16838

Pawar M, Sendoğdular ST, Gouma P (2018) A brief overview of TiO2 photocatalyst for organic dye remediation: case study of reaction mechanisms involved in Ce-TiO2 photocatalysts system. J Nanomater 2018.https://doi.org/10.1155/2018/5953609

Qamar MA, Shahid S, Javed M et al (2020) Highly efficient g-C3N4/Cr-ZnO nanocomposites with superior photocatalytic and antibacterial activity. J Photochem Photobiol A Chem 401:112776. https://doi.org/10.1016/J.JPHOTOCHEM.2020.112776

Ragupathi V, Panigrahi P, Ganapathi Subramaniam N (2020) Bandgap engineering in graphitic carbon nitride: effect of precursors. Optik (stuttg) 202:163601. https://doi.org/10.1016/J.IJLEO.2019.163601

Rattan Paul D, Nehra SP (2021a) Graphitic carbon nitride: a sustainable photocatalyst for organic pollutant degradation and antibacterial applications. Environ Sci Pollut Res 28:3888–3896. https://doi.org/10.1007/S11356-020-09432-6/TABLES/3

Reddy Yadav LS, Manjunath K, Archana B, et al (2016) Fruit juice extract mediated synthesis of CeO2 nanoparticles for antibacterial and photocatalytic activities. Eur Phys J Plus 131.https://doi.org/10.1140/EPJP/I2016-16154-Y

Retamoso C, Escalona N, González M et al (2019) Effect of particle size on the photocatalytic activity of modified rutile sand (TiO2) for the discoloration of methylene blue in water. J Photochem Photobiol A Chem 378:136–141. https://doi.org/10.1016/J.JPHOTOCHEM.2019.04.021

Saravanakumar K, Karthik R, Chen SM et al (2017) Construction of novel Pd/CeO2/g-C3N4 nanocomposites as efficient visible-light photocatalysts for hexavalent chromium detoxification. J Colloid Interface Sci 504:514–526. https://doi.org/10.1016/J.JCIS.2017.06.003

Sharma G, Prema D, Venkataprasanna KS et al (2020) Photo induced antibacterial activity of CeO2/GO against wound pathogens. Arab J Chem 13:7680–7694. https://doi.org/10.1016/J.ARABJC.2020.09.004

Sharma R, Almáši M, Nehra SP et al (2022) Photocatalytic hydrogen production using graphitic carbon nitride (GCN): a precise review. Renew Sustain Energy Rev 168:112776. https://doi.org/10.1016/J.RSER.2022.112776

Sher M, Javed M, Shahid S et al (2021) The controlled synthesis of g-C3N4/Cd-doped ZnO nanocomposites as potential photocatalysts for the disinfection and degradation of organic pollutants under visible light irradiation. RSC Adv 11:2025–2039. https://doi.org/10.1039/D0RA08573A

Song XZ, Zhu WY, Wang XF, Tan Z (2021) Recent advances of CeO2-based electrocatalysts for oxygen and hydrogen evolution as well as nitrogen reduction. ChemElectroChem 8:996–1020. https://doi.org/10.1002/CELC.202001614

Subashini A, Varun Prasath P, Sagadevan S, et al (2021) Enhanced photocatalytic degradation efficiency of graphitic carbon nitride-loaded CeO2 nanoparticles. Chem Phys Lett 769.https://doi.org/10.1016/j.cplett.2021.138441

Sun C, Sun C, Li H et al (2005) Controlled synthesis of CeO2 nanorods by a solvothermal method. Nanotechnology 16:1454–1463. https://doi.org/10.1088/0957-4484/16/9/006

Sun L, Du T, Hu C et al (2017) Antibacterial activity of graphene oxide/g-C3N4 composite through photocatalytic disinfection under visible light. ACS Sustain Chem Eng 5:8693–8701. https://doi.org/10.1021/ACSSUSCHEMENG.7B01431/SUPPL_FILE/SC7B01431_SI_001.PDF

Tan L, Xu J, Zhang X et al (2015) Synthesis of g-C 3 N 4 /CeO 2 nanocomposites with improved catalytic activity on the thermal decomposition of ammonium perchlorate. Appl Surf Sci 356:447–453. https://doi.org/10.1016/J.APSUSC.2015.08.078

Tang ZR, Zhang Y, Xu YJ (2011) A facile and high-yield approach to synthesize one-dimensional CeO 2 nanotubes with well-shaped hollow interior as a photocatalyst for degradation of toxic pollutants. RSC Adv 1:1772–1777. https://doi.org/10.1039/C1RA00518A

Wang Y, Shi R, Lin J, Zhu Y (2011) Enhancement of photocurrent and photocatalytic activity of ZnO hybridized with graphite-like C3N4. Energy Environ Sci 4:2922–2929. https://doi.org/10.1039/C0EE00825G

Wu P, Wang J, Zhao J et al (2014) Structure defects in g-C3N4 limit visible light driven hydrogen evolution and photovoltage. J Mater Chem A 2:20338–20344. https://doi.org/10.1039/C4TA04100C

Yan SC, Li ZS, Zou ZG (2010) Photodegradation of rhodamine B and methyl orange over boron-doped g-C3N4 under visible light irradiation. Langmuir 26:3894–3901. https://doi.org/10.1021/LA904023J

Yuan Y, Zhang L, Xing J et al (2015) High-yield synthesis and optical properties of g-C3N4. Nanoscale 7:12343–12350. https://doi.org/10.1039/C5NR02905H

Zou J, Wu S, Liu Y et al (2018) An ultra-sensitive electrochemical sensor based on 2D g-C3N4/CuO nanocomposites for dopamine detection. Carbon N Y 130:652–663. https://doi.org/10.1016/J.CARBON.2018.01.008